

Revised ephemeris and orbital period derivative of the supersoft X-ray source CAL 87 based on 34 years of observations

P. E. Stecchini^{1,2*}, F. Jablonski², M. P. Diaz¹, F. D’Amico², A. S. Oliveira³, N. Palivanas³ and R. K. Saito⁴

¹IAG, Universidade de São Paulo, Rua do Matão 1226, 05508–900, São Paulo–SP, Brazil

²Divisão de Astrofísica, Coordenação de Engenharia, Tecnologia e Ciências Espaciais, Instituto Nacional de Pesquisas Espaciais, Av. dos Astronautas 1758, 12227-010, S.J. Campos–SP, Brazil

³IP&D, Universidade do Vale do Paraíba, Av. Shishima Hifumi, 2911, 12244-000, S.J. Campos–SP, Brazil

⁴Departamento de Física, Universidade Federal de Santa Catarina, Trindade 88040-900, Florianópolis–SC, Brazil

Accepted XXX. Received YYY; in original form ZZZ

ABSTRACT

In this study, we present an analysis of over 34 years of observational data from CAL 87, an eclipsing supersoft X-ray source. The primary aim of our study, which combines previously analysed measurements as well as unexplored publicly available datasets, is to examine the orbital period evolution of CAL 87. After meticulously and consistently determining the eclipse timings, we constructed an O–C (observed minus calculated) diagram using a total of 38 data points. Our results provide confirmation of a positive derivative in the system’s orbital period, with a determined value of $\dot{P} = +8.18 \pm 1.46 \times 10^{-11}$ s/s. We observe a noticeable jitter in the eclipse timings and additionally identify a systematic delay in the X-ray eclipses compared to those observed in longer wavelengths. We discuss the interplay of the pertinent factors that could contribute to a positive period derivative and the inherent variability in the eclipses.

Key words: stars: individual: CAL 87 – white dwarfs – X-rays: binaries.

1 INTRODUCTION

Supersoft X-ray sources (SSSs) are characterized by their very soft emission in X-rays (below ~ 1 keV), blackbody-like spectra of effective temperatures $kT \sim 20$ –100 eV and high bolometric luminosities of $\sim 10^{36}$ – 38 erg s^{−1} (e.g. Kahabka & van den Heuvel 1997). van den Heuvel et al. (1992) showed that the soft X-ray emission observed in SSSs originates from stable hydrogen burning on the surface of a massive ($\gtrsim 1 M_{\odot}$) white dwarf (WD) which accretes at very high rates ($\sim 10^{-7} M_{\odot}$ year^{−1}) from its companion. For this high mass accretion to be sustained, argued van den Heuvel et al. (1992), the companion star (with mass M_2) of the binary system should be even more massive than the WD (M_1), i.e. a mass ratio $M_2/M_1 = q > 1$, which would lead to dynamically unstable mass transfer via Roche lobe overflow (RLOF). An alternative scenario was proposed by van Teeseling & King (1998), in which wind-driven mass transfer (WDMT) could also account for the high accretion rates in systems where the companion star is less massive, i.e. $q < 1$. This would also explain SSSs with orbital periods shorter than ~ 6 hr.

CAL 87 is a well known SSS located in the Large Magellanic Cloud (LMC). It was, along with CAL 83, the first supersoft object detected (Long et al. 1981), considered thus to be a prototype of the class. By placing observational parameters obtained from X-ray spectral analyses of CAL 87 in a luminosity-temperature diagram,

computed for surface hydrogen-burning WDs, Starrfield et al. (2004) inferred that the WD in the system might be as massive as $1.35 M_{\odot}$. Optical spectroscopic data revealed Balmer absorption lines whose radial velocities suggest that – for a 1.3 – $1.4 M_{\odot}$ compact object – the donor should have no more than $0.4 M_{\odot}$ (Hutchings et al. 1998). An orbital evolutionary analysis performed by Oliveira & Steiner (2007) pointed to a $0.34 M_{\odot}$ donor, corroborating the low mass nature of the companion star in CAL 87. These values lead to a mass ratio of $q \approx 0.25$ – 0.3 .

Light curve analyses have shown that CAL 87 exhibits partial eclipses in optical, (Callanan et al. 1989; Cowley et al. 1990; Alcock et al. 1997; Oliveira & Steiner 2007), ultraviolet (UV, Hutchings et al. 1995), and X-rays (Schmidtke et al. 1993; Asai et al. 1998; Greiner et al. 2004; Ebisawa et al. 2010) with a period of approximately 0.44 d (10.6 h). The depths of the eclipses imply a high orbital inclination ($> 70^{\circ}$, e.g. Schandl et al. 1997). An increase in the system’s orbital period ($\dot{P} = +1.7 \pm 0.3 \times 10^{-10}$ s/s) was reported by Oliveira & Steiner (2007) based on an estimation from two optical minima that were approximately 9000 cycles apart. Ribeiro et al. (2014) also derived a positive value ($\dot{P} = +6 \pm 2 \times 10^{-10}$ s/s) from the X-ray eclipse phase shift (relative to longer wavelengths) present in *XMM-Newton*’s data of CAL 87. The authors of both aforementioned studies have advocated that the increasing orbital period, coupled with the low mass ratio, favours the WDMT model; Ablimit & Li (2015) demonstrated through analytical and numerical calculations of orbital evolution that the reported dynamical parameters of CAL 87 indeed admit such a scenario.

* E-mail: paulo.stecchini@usp.br / paulo.stecchini@inpe.br

In this study, we compiled archival data spanning a 34-year time baseline for CAL 87. The primary goal of this compilation was the construction of an O–C (observed minus calculated) diagram, which serves as the basis for a comprehensive analysis of orbital period variations and other related phenomena. While certain datasets have been previously analysed, our approach includes several previously unexamined light curves, rendering them novel in the context of this investigation.

2 DATA COLLECTION AND DETERMINATION OF ECLIPSE TIMINGS

The times of minimum were essentially obtained through two different approaches: taken from published ephemerides or determined by us after analysing publicly available data. In the latter case, the data points used to build the light curves are sourced from either previously published measurements or archival data publicly available in survey/project catalogues.

Eclipse timings seized directly from published works are those from CTIO (one minimum – B, V and R bands altogether; Cowley et al. 1990), ESO & SAAO (one minimum – B and V bands altogether; Callanan et al. 1989), and SOAR (V band; Oliveira & Steiner 2007). They are marked with an asterisk in Table 1. The HST (UV band) and a second CTIO (V band) minima were determined based on measurements presented in table 1 of Hutchings et al. (1995) and table 2 of Hutchings et al. (1998), respectively.

All other datasets were collected from public catalogues. These are the light curves from MACHO¹ (two minima – a "blue" and a "red" band), OGLE² (two minima, a V and a I band), VMC³ (one minimum – Y, J, K_S bands altogether), and TESS⁴ (28 minima, in a wide I band). Except for TESS (which will be explained shortly), the aforementioned data were straightforwardly retrieved as magnitudes versus time. Data from MACHO had already been analysed by Alcock et al. (1997), who reported the ephemeris $T_{0, \text{Alcock}} = \text{MJD } 50111.0144(3) + 0.44267714(6)$, most commonly cited up to the present day.

The TESS light curves were produced from aperture photometry on the Full Frame Images (FFIs) of 31 sectors. Each sector spans about 26 days of observations, at a cadence of 30, 10, or 3 minutes. Three of the sectors were discarded due to the target being too close to the edge of the detector. The aperture photometry was performed with Lightkurve (Lightkurve Collaboration et al. 2018), an open source Python package written for TESS and Kepler data analysis. From each FFI we made a 11×11 pixels cutout centred on the target. The light curves were obtained from those cutouts by measuring the total flux in a 2×2 pixel mask that includes the target, subtracted of the sky average flux obtained from a background mask. The resulting data are given in flux ($e^- s^{-1}$) versus Barycentric Tess Julian Date (BTJD), defined as $\text{BTJD} = \text{BJD} - 2,457,000$, where BJD is the Barycentric Julian Date.

Some of the data have not been previously mentioned in the literature; this applies to the measurements of CAL 87 from OGLE,

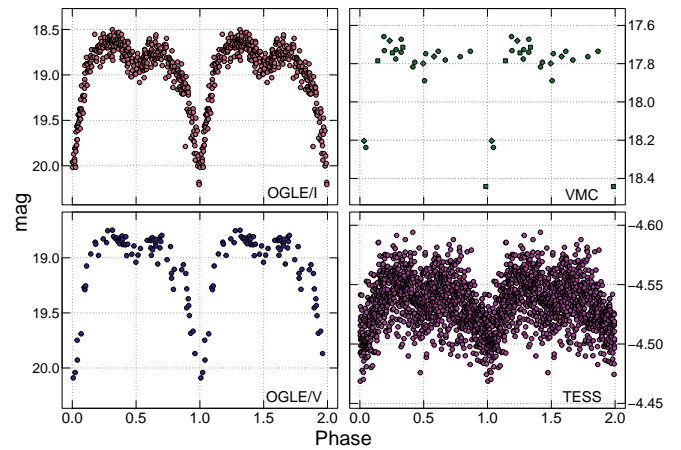


Figure 1. Folded light curves of CAL 87 from archival data not previously analysed. The light curves are folded with the linear ephemeris presented in equation 1 (Section 3). Two cycles are shown for clarity. OGLE data (left panels): vertical axes show the actual magnitude measured in bands I (upper) and V (bottom). VMC data (upper right panel): circles, squares and diamonds refer, respectively, to measurements in bands K_S, Y and J. Vertical axis shows magnitude for K_S; the Y and J data points were shifted to match the K_S level out of eclipse. TESS (sector 11) data (bottom right panel): straightforwardly converted from flux to magnitude ($-2.5 \log f$), i.e. the actual units for the vertical axis are Δmag . The relatively small amplitude and large scatter are due to light dilution caused by the presence of numerous other sources within the TESS 2×2 pixels extraction aperture where CAL 87 is found.

VMC and TESS. Their folded light curves are displayed in Fig. 1. For TESS, from which we use data from multiple sectors and thus obtain multiple eclipsing times, we present the light curve from one sector.

While our primary focus was not on incorporating X-ray eclipses into the period evolution analysis, we retrieved historical X-ray light curves to examine their correlation with those at longer wavelengths. X-ray data reduction and light curves production were accomplished following each mission's standard procedures: XSELECT tasks from the FTOOLS package (HEASOFT, v. 6.32) for PSPC data from ROSAT, the Chandra Interactive Analysis of Observations (CIAO, v. 4.15.0) for ACIS-S data from Chandra, and the XMM–Newton Science Analysis System (SAS, v. 20.0.0) for EPIC-pn data from XMM–Newton. All light curves were extracted for the energy band 0.2–1 keV. ROSAT's observation spanned over 60 hours, although there were numerous gaps. Chandra and XMM–Newton observations of CAL 87 were continuous over more than one orbital cycle, encompassing 3 and 2 full eclipses, respectively. The phase diagrams for the X-ray data are presented in Fig. 3 later in this paper.

To determine a composite time of minimum for each dataset, we started with a provisional epoch close to the middle of the dataset. The precise time of minimum was extracted with respect to this epoch using a spline fit with the aid of the `loess()` function in the R statistical package. To estimate the uncertainty in the derived time of minimum, a bootstrap technique was employed. This technique involves resampling each flux value around its nominal value based on the corresponding $1-\sigma$ error bar. The median of the absolute deviations from one thousand realisations of this procedure was used to calculate the standard deviation of the timing. In Table 1 we present the final epochs of minimum and their uncertainties, keeping the cycle number relative to the ephemeris of Alcock et al. (1997), and general information regarding the observations. For brevity, all the

¹ <http://cdsarc.u-strasbg.fr/viz-bin/VizieR-5?-ref=VIZ642dda8b315c&-out.add=&-source=II/247/machovar&recno=4458>

² <https://ogledb.astrouw.edu.pl/~ogle/OCVS/?OGLE-LMC-ECL-24119>

³ https://archive.eso.org/scienceportal/home?data_collection=VMC

⁴ <https://mast.stsci.edu>

Table 1. Epochs of minimum.

Epoch of minimum (MJD)	Uncertainty in epoch (days)	Cycle [†]	Provenance	Band
47506.30210*	0.0002	-5884	CTIO	B, V, R
47531.09520*	0.0030	-5828	ESO & SAAO	B, V
48306.67950	0.0110	-4076	ROSAT	X-rays ^a
49724.11870	0.0060	-874	HST	UV ^b
50028.23574	0.0024	-187	CTIO	V
50180.51280	0.0015	157	MACHO	b ^c
50182.72351	0.0019	162	MACHO	r ^d
52135.38977	0.0079	4573	Chandra	X-rays
52748.49518	0.0014	5958	XMM-Newton	X-rays
53680.32440*	0.0003	8063	SOAR	V
56001.28307	0.0021	13306	OGLE	I
56022.53521	0.0011	13354	OGLE	V
56632.97981	0.0060	14733	VMV	Y, J, K _s
58338.62551	0.0039	18586	TESS	Wide I ^e
58367.39827	0.0019	18651	TESS	Wide I
58423.17168	0.0040	18777	TESS	Wide I
58450.17719	0.0051	18838	TESS	Wide I
58478.51156	0.0053	18902	TESS	Wide I
58503.30069	0.0042	18958	TESS	Wide I
58529.42007	0.0056	19017	TESS	Wide I
58555.53251	0.0029	19076	TESS	Wide I
58582.09385	0.0025	19136	TESS	Wide I
58609.99029	0.0042	19199	TESS	Wide I
58638.76056	0.0042	19264	TESS	Wide I
59047.79394	0.0053	20188	TESS	Wide I
59073.91511	0.0046	20247	TESS	Wide I
59100.91171	0.0046	20308	TESS	Wide I
59156.68956	0.0036	20434	TESS	Wide I
59186.79344	0.0040	20502	TESS	Wide I
59241.25008	0.0034	20625	TESS	Wide I
59267.37093	0.0024	20684	TESS	Wide I
59293.48852	0.0033	20743	TESS	Wide I
59319.60339	0.0043	20802	TESS	Wide I
59346.60482	0.0045	20863	TESS	Wide I
59375.37238	0.0020	20928	TESS	Wide I
59975.20202	0.0019	22283	TESS	Wide I
60000.88383	0.0043	22341	TESS	Wide I
60026.99755	0.0037	22400	TESS	Wide I
60053.99849	0.0016	22461	TESS	Wide I
60081.89137	0.0054	22524	TESS	Wide I
60110.22337	0.0056	22588	TESS	Wide I

*Epochs taken from the literature.

[†]Based on the cycle counting of Alcock et al. (1997).

^a0.2–1.0 keV. ^b1350–2200 Å. ^c~V. ^d~R+I. ^e~6000–10000 Å.

time stamps are expressed in MJD (Modified Julian Date), i.e. HJD or BJD – 2,400,000.5.

3 THE O–C DIAGRAM FOR CAL 87

The best-fitting weighted linear ephemeris ($T_{\min} = T_0 + P_0 E$), calculated when considering all epochs of minimum listed in Table 1 – except for the X-ray data – is

$$T_{\min} = \text{MJD } 50111.01655(28) \pm 0.442677572(33) E, \quad (1)$$

where E is the number of elapsed cycles since T_0 .

To investigate a potential orbital period derivative (\dot{P}), we incorporated a quadratic term in the ephemeris using the well-known

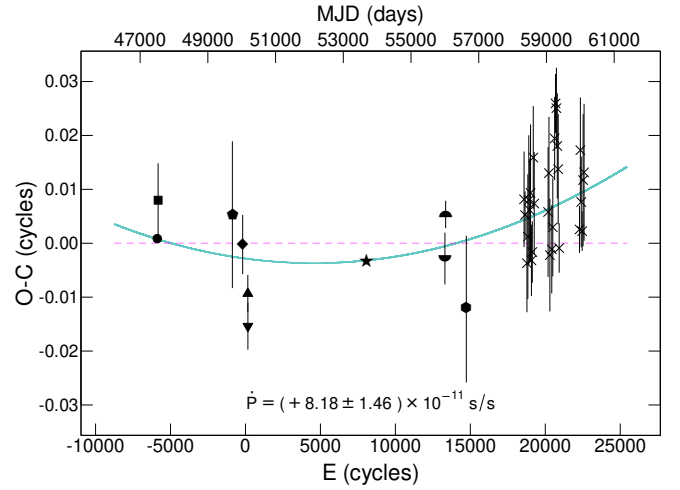


Figure 2. O–C diagram computed for the data presented in Table 1 (except for the X-ray data). Both computations incorporated the uncertainties of the measurements as weighting factors. Vertical error bars are shown for all data points, although in some cases the bars are smaller than the symbols representing them. Circle: epoch taken from Cowley et al. (1990); square: epoch taken from Callanan et al. (1989); pentagon: HST/UV data, taken from Hutchings et al. (1995); diamond: CTIO data, taken from Hutchings et al. (1998); up-pointing triangle: MACHO/b; down-pointing triangle: MACHO/r; star: epoch taken from Oliveira & Steiner (2007); top half circle: OGLE/I; bottom half circle: OGLE/V; hexagon: VMV; crosses: TESS. Dashed magenta line and solid green line are linear and quadratic fits, respectively. The fits keep the cycle counting of Alcock et al. (1997).

Taylor expansion (i.e. $T_{\min} = T_0 + P_0 E + \frac{1}{2} P_0 \dot{P} E^2$, keeping the same notation). The resulting weighted parabolic fit yields

$$T_{\min} = \text{MJD } 50111.01530(13) + 0.442677407(34) E + 1.81(32) \times 10^{-11} E^2, \quad (2)$$

which translates to a time derivative of $\dot{P} = +8.18 \pm 1.46 \times 10^{-11}$ s/s. Employing the reduced chi-squared ($\chi_{\text{red}}^2 = \chi^2/\nu$, where χ^2 denotes the standard chi-square statistic and ν represents the degrees of freedom) as a measure of goodness of fit, we obtain $\chi_{\text{red}}^2 = \frac{49.49}{36} = 1.37$ and $\chi_{\text{red}}^2 = \frac{37.46}{35} = 1.07$ for the linear and quadratic fits, respectively. Both an F-test and a χ^2 difference test show that there is less than a 0.1% probability that the null hypothesis (i.e. the linear model) is the best choice. Moreover, upon computing the Akaike Weight (Akaike 1978), which expresses the likelihood of a model best representing the data among a set of models, we find that the parabolic model is approximately 99% more plausible in describing the evolution of CAL 87’s epochs of minimum. The data, along with the linear and quadratic fits, are presented in Fig. 2 in the form of an O–C diagram.

We have excluded X-ray eclipsing times from the O–C calculation based on a previous hint that they may not precisely coincide with the optical eclipse. Ebisawa et al. (2010), in their analysis of the XMM-Newton observation of CAL 87 (which we also employ here), reported a $\sim 0.03 \phi$ delay compared to the ephemeris of Alcock et al. (1997). Indeed, the weighted average of the residuals for the three X-ray minima analysed here (see Table 1), relative to those predicted by equation 2, is 0.02 ± 0.01 . For clarity and visualization of such a delay, we present in Fig. 3 the phase diagram of the three X-ray (0.2–1 keV) light curves (ROSAT/PSPC, Chandra/ACIS, and XMM-Newton/pn), as well as that of MACHO/b, i.e. in the optical band. They are folded according to the linear ephemeris of equation (1).

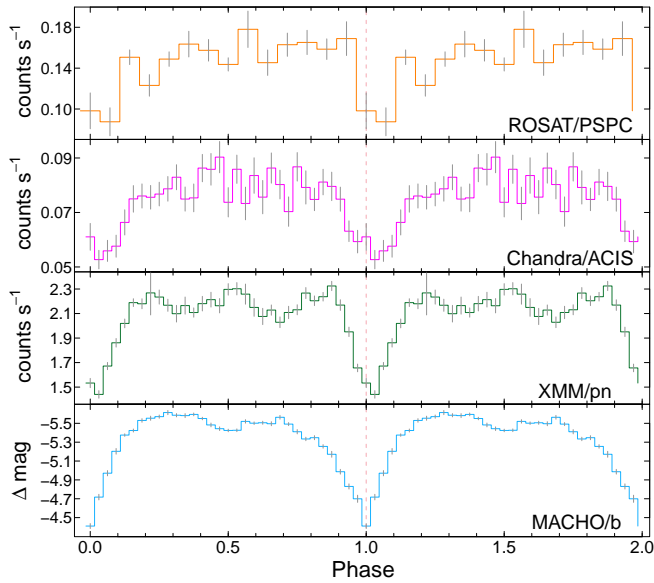


Figure 3. Phase diagrams of CAL 87 to evince the displacement of the X-ray (0.2–1 keV; first, second and third panels) eclipse minimum time relative to longer wavelengths (optical; bottom panel). Light curves were folded according to the linear ephemeris presented in equation (1). Two cycles are shown for clarity. Binning consists of 32 bins per phase, except for *ROSAT* (first panel), in which only 14 bins per phase were used due to the uneven distribution of data throughout an orbital cycle.

The observation gaps in *ROSAT*’s data prevented sufficient coverage of all orbital phases; as a result, its folded light curve has a coarser binning (14 bins per phase) compared to the other three, which have 32 bins per phase. We have not attempted to derive an ephemeris for the X-ray eclipses alone due to i) the small number of data points to fit a parabola, ii) the minima’s relatively large uncertainties, and iii) their irregular distribution along the time baseline (*XMM-Newton* and *Chandra* timings too close and *ROSAT* timing about 10000 cycles apart).

At last, to facilitate assessment of the differences in shape of the light curves of CAL 87 in X-rays and optical, we present again the phase diagrams of *XMM-Newton* and MACHO superimposed in Fig. 4. For a clearer comparison, MACHO magnitudes have been converted to flux by simply calculating $10^{(-0.4 \times \text{mag})}$, and the flux values of both have then been rescaled to ensure the same range between minimum and maximum. Also, the X-ray minimum has been adjusted to align in phase with the optical minimum.

4 DISCUSSION AND CONCLUSIONS

Conspicuous differences between the eclipse profiles in the optical/IR and X-rays are found. The eclipse seems to display opposite asymmetries: its ingress is prolonged in the optical/IR and steeper in X-rays, whereas the egress is slower than the ingress in X-rays (Fig. 4). In addition to the profiles, the X-ray minimum is observed to be delayed compared to the optical (Fig. 3). These differences indicate that the corresponding sources are not equally distributed around the WD. For instance, if the major contribution to X-rays is associated with the disk-WD boundary layer then the true geometrical conjunction is around phase 0.02. If that is the case, such a change in absolute phasing should be taken into account when deriving binary dynamical solutions from eclipse-phased radial velocity measurements. On

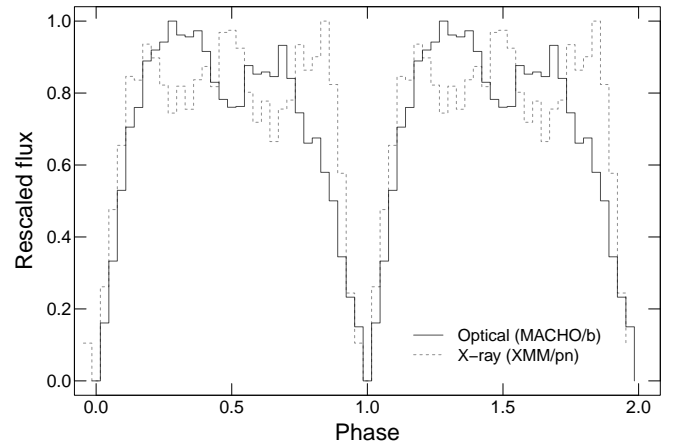


Figure 4. Optical (black solid line) and X-ray (dashed grey line) phase diagrams of CAL 87, superimposed to highlight shape differences. For comparison purposes, the optical magnitudes have been converted to flux, and the flux values of both light curves have been rescaled to share the same minimum and maximum values. Additionally, the X-ray minimum, originally delayed with respect to the optical (Fig. 3), has been adjusted to match the optical minimum.

the other hand, the eclipse timings used in the optical O–C diagram (Table 1) have well defined uncertainties. When phased, they exhibit a notable phase jitter (Fig. 2), suggesting an inherently variable phase of minimum light, by a few degrees. One may conjecture that variable asymmetries in the disk’s optical emission or in an optically thick wind might explain these small shifts in minimum phase (e.g. Meyer-Hofmeister et al. 1997). An anti-correlation between the optical and X-ray flux around phase 0.5 becomes apparent upon comparing the phase-folded curves in Fig. 3, specially from MACHO and *XMM-Newton* data (e.g. Pearson correlation coefficient of -0.59 within phases 0.35 and 0.65; see also Fig. 4), which could be related to the contrasting eclipse asymmetry. Such anti-correlation is less clear for *ROSAT* or *Chandra* light curves, perhaps due to poorer photon statistics. Additional simultaneous multiwavelength observations are required to confirm and quantify this behavior, which has also been seen in other SSSs (e.g. CAL 83, Stecchini et al. 2023).

In order to evaluate the secular binary period evolution it is important to quantify the period change using the most extensive time baseline available. Low-frequency noise in O–C diagrams of accreting systems can mislead the observer towards a spurious, yet statistically significant, \dot{P} value.

The observed long-term positive \dot{P} for this system serves as a probe to elucidate the roles of winds, angular momentum losses, and mass ratio in SSSs. Accretion onto the white dwarf may occur via Roche lobe overflow (RLOF) or via wind from a detached irradiated companion. In the context of non-conservative mass transfer, a well-established dynamical relation exists between \dot{P}/P , the mass loss rate, M_1 , M_2 , the primary accretion rate, and, for long-period systems, the efficiency of magnetic braking, in the case of a circular orbit (e.g. Hilditch 2001). Radiation driven winds are expected to emerge from both the luminous WD’s photosphere and the irradiated companion. These winds carry both mass and angular momentum, with the former contributing positively to \dot{P} . Magnetic braking, even in a weak wind from the companion star, introduces a negative contribution. The process of accretion onto the WD itself plays a major role, resulting in either a negative or positive term depending on whether the donor is more massive or less massive than the WD. Our determination

of the period derivative favours the hypothesis of mass loss and/or a lighter donor relative to the accreting object. A positive \dot{P} was previously identified for CAL 87 by Oliveira & Steiner (2007), who suggested that the system is powered by the companion wind (the WDMT model) instead of RLOF. Ribeiro et al. (2014) also reported a positive period derivative, which was larger than our value, using a small number of X-ray eclipse timings.

Curiously, the SSS-like binary V Sge (Steiner & Diaz 1998), which has a comparably long orbital period, seems to exhibit a distinct mass transfer/wind regime. A decreasing orbital period has been claimed for this eclipsing system (Patterson et al. 1998; Zang et al. 2022), suggesting a RLOF, high mass transfer rate from the donor. WX Cen, another binary system of the V Sge class (Diaz & Steiner 1995; Oliveira & Steiner 2004), also shows an orbital period with a negative time derivative (Zang, Qian, & Fernández-Lajús 2023). In this case, the secondary component is likely less massive than the WD, and thus angular momentum loss driven by a magnetic wind has been proposed as the mechanism for the orbital evolution. In contrast, V617 Sgr, also known as a V Sge-type eclipsing system, exhibits a positive \dot{P} (Steiner et al. 2006; Zang et al. 2023) with the same order of magnitude as found for CAL 87. A positive \dot{P} is also observed in the long-period eclipsing SSS QR And (Zang, Qian, & Fernández-Lajús 2023), which presents an optical orbital light curve remarkably similar to that of CAL 87.

Revised dynamical constraints on stellar masses, well-defined long-term period derivatives, and limits on system mass loss are essential for a more accurate understanding of the mass transfer modes in SSSs. These fundamental quantities remain uncertain or unknown for nearly all bona fide SSSs.

ACKNOWLEDGEMENTS

PES acknowledges Conselho Nacional de Desenvolvimento Científico e Tecnológico (CNPq) for financial support under PCI/INPE grant #317428/2023-3. MPD thanks support from CNPq under grant #305033. ASO acknowledges São Paulo Research Foundation (FAPESP) for financial support under grant #2017/20309-7. NP thanks support from Coordenação de Aperfeiçoamento de Pessoal de Nível Superior (CAPES) under grant #88887.823264/2023-00. R.K.S. acknowledges support from CNPq through projects #308298/2022-5 and #350104/2022-0. PES, FJ and FD also thank Agência Espacial Brasileira (AEB). The authors thank an anonymous referee for her/his helpful comments and suggestions.

This research is partially based on observations taken within the ESO Public Survey VMC, Programme ID 179.B-2003. This paper also includes data collected by the TESS mission, which are publicly available from the Mikulski Archive for Space Telescopes (MAST). Funding for the TESS mission is provided by the NASA's Science Mission Directorate. This research made use of Lightkurve, a Python package for Kepler and TESS data analysis (Lightkurve Collaboration et al. 2018).

DATA AVAILABILITY

The data underlying this article are public; the references and/or paths to access are provided in the main text.

REFERENCES

Ablimit, I. & Li, X.-D. 2015, *ApJ*, 815, 17. doi:10.1088/0004-637X/815/1/17

- Akaike, H. 1978, *Annals of the Institute of Statistical Mathematics*, 30, 9
- Alcock, C., Allsman, R. A., Alves, D. R., et al. 1997, *MNRAS*, 287, 699. doi:10.1093/mnras/287.3.699
- Asai, K., Dotani, T., Nagase, F., et al. 1998, *ApJ*, 503, L143. doi:10.1086/311547
- Callanan, P. J., Machin, G., Naylor, T., et al. 1989, *MNRAS*, 241, 37P. doi:10.1093/mnras/241.1.37P
- Cowley, A. P., Schmidtke, P. C., Crampton, D., et al. 1990, *ApJ*, 350, 288. doi:10.1086/168381
- Diaz M. P., Steiner J. E., 1995, *AJ*, 110, 1816. doi:10.1086/117653
- Ebisawa, K., Rauch, T., & Takei, D. 2010, *Astronomische Nachrichten*, 331, 152. doi:10.1002/asna.200911317
- Greiner, J., Iyudin, A., Jimenez-Garata, M., et al. 2004, *Revista Mexicana de Astronomia y Astrofisica Conference Series*, 20, 18. doi:10.48550/arXiv.astro-ph/0403426
- Hilditch R. W., 2001, *icbs.book*, 392
- Hutchings, J. B., Cowley, A. P., Schmidtke, P. C., et al. 1995, *AJ*, 110, 2394. doi:10.1086/117698
- Hutchings, J. B., Crampton, D., Cowley, A. P., et al. 1998, *ApJ*, 502, 408. doi:10.1086/305895
- Kahabka, P. & van den Heuvel, E. P. J. 1997, *ARA&A*, 35, 69. doi:10.1146/annurev.astro.35.1.69
- Lightkurve Collaboration, Cardoso J. V. de M., Hedges C., Gully-Santiago M., Saunders N., Cody A. M., Barclay T., et al., 2018, *ascl.soft.1812.013*
- Long, K. S., Helfand, D. J., & Grabelsky, D. A. 1981, *ApJ*, 248, 925. doi:10.1086/159222
- Meyer-Hofmeister, E., Schandl, S., & Meyer, F. 1997, *A&A*, 321, 245
- Oliveira A. S., Steiner J. E., 2004, *MNRAS*, 351, 685. doi:10.1111/j.1365-2966.2004.07817.x
- Oliveira, A. S. & Steiner, J. E. 2007, *A&A*, 472, L21. doi:10.1051/0004-6361:20077971
- Patterson, J., Kemp, J., Shambrook, A., et al. 1998, *PASP*, 110, 380. doi:10.1086/316147
- Ribeiro, T., Lopes de Oliveira, R., & Borges, B. W. 2014, *ApJ*, 792, 20. doi:10.1088/0004-637X/792/1/20
- Schandl, S., Meyer-Hofmeister, E., & Meyer, F. 1997, *A&A*, 318, 73
- Schmidtke, P. C., McGrath, T. K., Cowley, A. P., et al. 1993, *PASP*, 105, 863. doi:10.1086/133246
- Starrfield, S., Timmes, F. X., Hix, W. R., et al. 2004, *ApJ*, 612, L53. doi:10.1086/424513
- Stecchini, P. E., Perez Diaz, M., D'Amico, F., et al. 2023, *MNRAS*, 522, 3472. doi:10.1093/mnras/stad1144
- Steiner, J. E. & Diaz, M. P. 1998, *PASP*, 110, 276. doi:10.1086/316139
- Steiner, J. E., Oliveira, A. S., Cieslinski, D., et al. 2006, *A&A*, 447, L1. doi:10.1051/0004-6361:200500227
- van den Heuvel, E. P. J., Bhattacharya, D., Nomoto, K., et al. 1992, *AAP*, 262, 97
- van Teeseling, A. & King, A. R. 1998, *A&A*, 338, 957
- Zang L., Qian S., Fernández-Lajús E., 2023, *MNRAS*, 522, 2732. doi:10.1093/mnras/stad1161
- Zang L., Qian S., Fernández-Lajús E., 2023, *ApJ*, 944, 97. doi:10.3847/1538-4357/acb52f
- Zang L., Qian S., Zhu L., Liu L., 2022, *MNRAS*, 511, 553. doi:10.1093/mnras/stac047
- Zang L., Zhao E., Fernández-Lajús E., Zubairi A. W., Sarotsakulchai N., 2023, *NewA*, 103, 102054. doi:10.1016/j.newast.2023.102054

This paper has been typeset from a $\text{\TeX}/\text{\LaTeX}$ file prepared by the author.